CHAPTER 4

Lorentz Correction Factors

In the last chapter, it was demonstrated that electron diffraction amplitudes extracted from PED patterns with large precession angle ϕ can be used with direct methods to generate very good starting structure maps. The only processing necessary is high-pass filtering of low-index reflections. Multislice simulations showed that — for a much larger range of experimental thicknesses than conventional diffraction — PED data has low enough error such that it is sufficient for use with direct methods without modification. However, the simulations also showed that this is not the case for large thicknesses (> 50 nm), and a correction of the intensities would be required when the crystal is thick.

Precession electron diffraction is intended for finding initial starting structures from unknown materials, therefore in practice usually very little *a priori* information about the structure will be known when first investigating a novel material. The thickness is another piece of information that is almost always missing. Any practical correction factor must therefore be based upon a simple model that is highly tolerant of error within the input parameters. In other words, what is sought is a *well-conditioned* model.

While the structure of a novel material is not known, useful information is known about the characteristics of the PED experiment. First, the microscopist knows the geometry of the incident intensity, as well as where the major errors in the scattered intensities lie. Additionally, it may be possible to tell during the experiment whether the specimen spans a large range of thicknesses and/or is uniformly very thick using morphological clues (such as edge effects), thickness fringes, or the presence of diffuse scattering and/or Kikuchi lines. Finally, it is known that precession decreases dynamical coupling such that systematic paths are suppressed and, at any given time, usually only one beam is strongly excited. The simplest model that describes this is a model involving only two beams: the incident and a scattered beam.

In this chapter, the correction factors based upon two-beam approximations will be investigated in detail to understand how they work and when it is appropriate to apply them. The results will also give some new insight into how PED itself works. Some of the contents will be a more accurate reworking of the analysis previously done by Gjønnes (1997) and Vincent and Midgley (1994). First, an exact geometrical model will be established that can be evaluated numerically. This will serve as a reference for comparison with the Gjønnes correction factors. It will initially take the form of a simple kinematical correction and then will be expanded to include dynamical two-beam effects. The distinction between the kinematical geometry portion

(Lorentz) and the dynamical portion will be discussed, then they will be compared to their analogues within the Gjønnes correction factors. Lastly, a comparison of these models to multislice simulation will be given, with the goal of finding the limits of where each model is applicable to real data.

The corrections based upon two-beam dynamical theory, while simple, require that the structure factorsalready be known. The term *forward calculation* will be used to describe this, meaning that correction requires the structure factors already be known, which — if they are previously known — negates the need for calculating the correction factors in the first place. Nevertheless, the investigations of the particular corrections described in this chapter help to elucidate the nature of PED and represent a much simpler model with which to describe the physics of precession than the calculation-intensive full dynamical multislice. Additionally, the tolerance for input error is investigated.

4.1. Derivation of Correction Factors

The similarities of PED to powder diffraction were recognized early on by Vincent and Midgley (1994), who proposed the first correction factor for PED in the first paper on PED. This was based upon a two-beam dynamical model intended for correcting powder diffraction intensities (Blackman 1939). This correction factor was revised by Gjønnes (1997) to better describe the geometrical effects and a number of variations of this factor have been used in the literature (Vincent and Midgley 1994; Gjønnes et al. 1998b,a; Midgley et al. 1998; Gemmi et al. 2003). The version of the Gjønnes correction factor intended for parallel illumination (analagous to the convergent form of the Gjønnes factor in equation 1.30) is

$$I_g^{kin} \propto I_g^{corr} = \left(\mathbf{g}\sqrt{1 - \left(\frac{\mathbf{g}}{2R_0}\right)} \frac{A_{\mathbf{g}}}{\displaystyle\int_0^{A_{\mathbf{g}}} J_0(x)dx} \right) I_g^{exp}, \tag{4.1}$$

where $\mathbf{g}$ is the reflection vector and $A_{\mathbf{g}} = \frac{2\pi t U_{\mathbf{g}}}{k}$ (as defined in Gjønnes et al. (1998a)). In the definition of $A_{\mathbf{g}}$, t is the specimen thickness in Ångströms, $U_{\mathbf{g}}$ is the structure factor, and k is the wavevector magnitude of the incident radiation. Equation 4.1 represents two corrections: 1) a pre-factor to correct for geometry (Lorentz portion) and 2) a two-beam dynamical correction (Blackman portion).

There are two problems with equation 4.1. First note that the value of $A_{\mathbf{g}}$, which must be defined absolutely, is critical for calculating the correct value of the integrated intensity. As pointed out in section 1.4.2, the argument of the integrand in equation 4.1 is different from that used in the Blackman formula (equation 1.24) by a factor of two, altering the periodicity of the Bessel function J_0. The forms of $A_{\mathbf{g}}$ used in Gjønnes (1997) and Gjønnes et al. (1998b) had conflicting definitions and, furthermore, the structure factors ($U_{\mathbf{g}}$) that were used to define $A_{\mathbf{g}}$ had not been clearly defined. Without knowledge of the pre-factor constants, the correctness of $A_{\mathbf{g}}$ in these studies is not certain. The second problem is that an assumption has been made that the geometry effects can be separated from the dynamical scattering effects. The conditions for this approximation to hold were not specified in the derivation of the correction factor (Gjønnes 1997).

In this section, the correction will be re-derived using kinematical and two-beam electron diffraction theory. The re-derivation is more exact than the previous models and will be used to explore the limits of their approximation. For completeness, the original derivation by Blackman (1939) is included at the end of this section in section 4.1.3. The reader is referred to Gjønnes (1997) for the derivation of the Lorentz portion in equation 4.1.

4.1.1. Kinematical Precession

Recall from section 2.1 that the intensity measured in precession represents a finite integration of the scattered intensity. The relevant geometry, shown previously as figure 2.1, is reproduced here as figure 4.1. The intensity scattered by the crystal is the true intensity ${F_{\mathbf{g}}}^2$ multiplied by some function dependent upon specimen dimensions. Intensity is scattered when this shape function — which manifests in reciprocal space as a rod shape (relrod) — is intercepted by the Ewald sphere. The true intensity can also be recovered by dividing the measured intensity by the value of the shape function at the interception point, described by excitation error $\mathbf{s_g}$. Similarly, the true intensity can be recovered from the measured *integrated* intensity from PED by dividing by the integrated shape function, in other words

$$|F_{\mathbf{g}}|^2 \propto I_{\mathbf{g}}^{corr} = C(\mathbf{g}, t, \phi) I_{\mathbf{g}}^{exp}, \tag{4.2}$$

where $C_{\mathbf{g}}$ is inversely proportional to the precession integral of the shape function of the scattered intensity.

In this derivation, we seek to evaluate the integral of the scattered intensity over excitation error that occurs during the precession:

$$I_{\mathbf{g}}^{prec} = \int I_{\mathbf{g}}(\mathbf{s_g}) d\mathbf{s_g}. \tag{4.3}$$

Equation 4.3 is more conveniently treated as an integration over the precession variable θ representing the circuit traced by the Laue circle, given by

$$I_{\mathbf{g}}^{prec} = \int_0^{2\pi} I(\theta) d\theta. \tag{4.4}$$

The change of variables can be made starting from the equation of the Ewald sphere:

$$(x - \mathbf{k}_x)^2 + y^2 + (z - \mathbf{k}_z)^2 = \mathbf{k}^2, \tag{4.5}$$

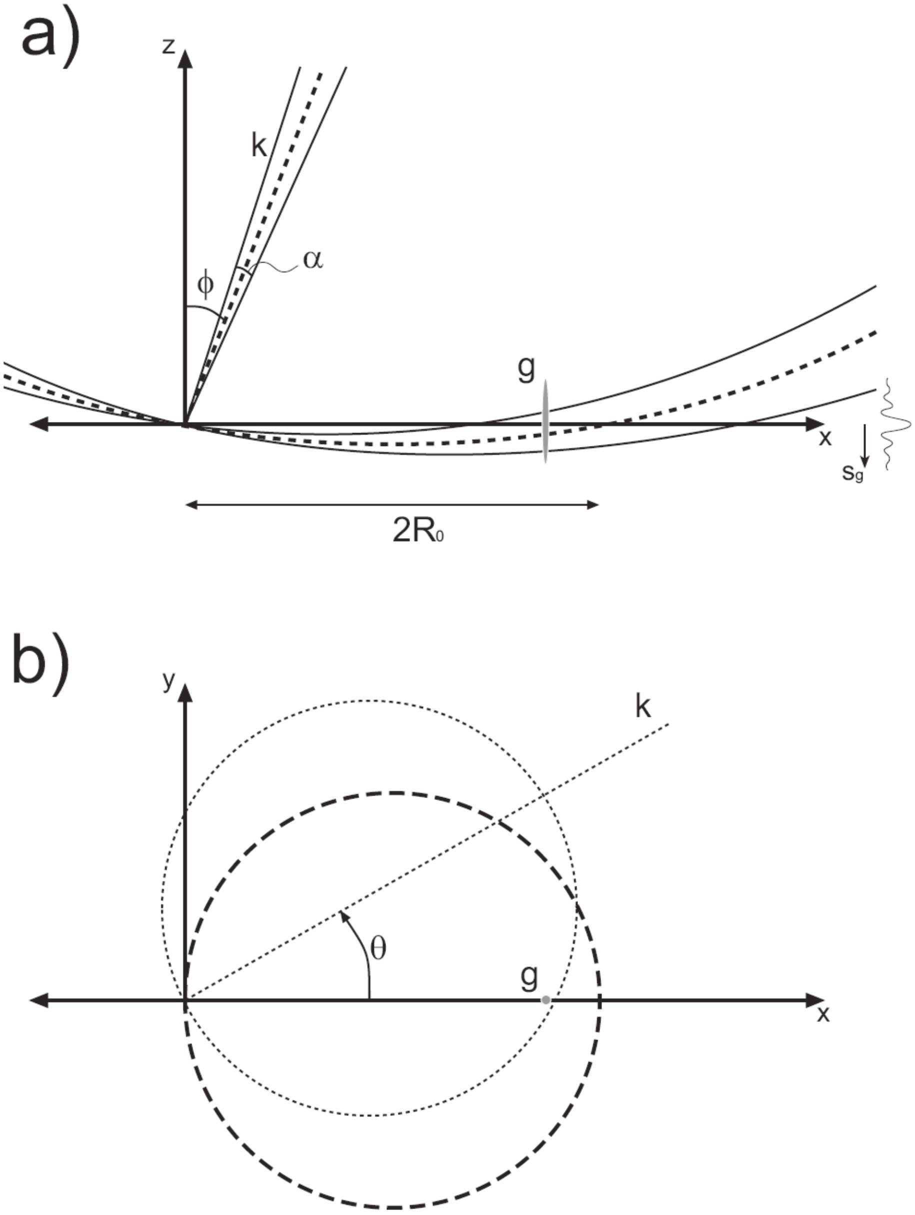

Figure 4.1. Reciprocal space geometry in (a) $x - y$ plane and (b) $x - z$ plane. The beam precesses about the z-axis maintaining constant ϕ. In (b), the ZOLZ (bold dashed circle) precesses about the z-axis.

where $\mathbf{k} = 1/\lambda$, and $\mathbf{k}_x$ and $\mathbf{k}_z$ represent the deviation of the Ewald sphere origin in x and z, respectively, due to precession. For a reflection $\mathbf{g}$ located at $(x, y) = (|\mathbf{g}|\cos\theta, |\mathbf{g}|\sin\theta)$, the Cartesian variables can be converted to functions of θ starting with the substitution

$$(\mathbf{g}\cos\theta - \mathbf{k}_x)^2 + (\mathbf{g}\sin\theta)^2 + (z - \mathbf{k}_z)^2 = \mathbf{k}^2. \tag{4.6}$$

Simplifying using geometric identities, substituting $\mathbf{s_g}$ for z, and utilizing $|\mathbf{k}_x|^2 + |\mathbf{k}_z|^2 = |\mathbf{k}|^2$, this reduces to

$$\mathbf{g}^2 - 2\mathbf{k}_x\mathbf{g}\cos\theta - 2k_z s_{\mathbf{g}} = 0, \tag{4.7}$$

where s^2 is very small and has been eliminated from the previous equation. Since $\mathbf{k}_z \approx \mathbf{k}$, and $\mathbf{k}_x \approx \mathbf{k}\phi$ in the limit of small ϕ, this is rearranged to get excitation error as a function of θ:

$$\mathbf{s_g}(\theta) = \frac{g^2 - 2k\phi g\cos\theta}{2k}. \tag{4.8}$$

In kinematical scattering theory, the relrods representing the scattered intensity are described by the inversion of the top hat function, therefore

$$I(\mathbf{s_g}) = \frac{1}{\xi_{\mathbf{g}}^2}\frac{\sin^2(\pi t s_{\mathbf{g}})}{{s_{\mathbf{g}}}^2}. \tag{4.9}$$

The characteristic length $\xi_{\mathbf{g}}$ (also called the extinction distance) is a function of the experimental variables structure factor $F_{\mathbf{g}}$, unit cell volume V_c, electron wavelength λ, and Bragg angle θ_B given by

$$\xi_{\mathbf{g}} = \frac{\pi V_c\cos\theta_B}{\lambda F_{\mathbf{g}}}. \tag{4.10}$$

The correction factor follows from equations 4.8 and 4.9, giving

$$\int_0^{2\pi} I(\theta)d\theta = \frac{1}{\xi_{\mathbf{g}}^2}\int_0^{2\pi}\frac{\sin^2\left\{\pi t\left(\frac{g^2-2k\phi g\cos\theta}{2k}\right)\right\}}{\left(\frac{g^2-2k\phi g\cos\theta}{2k}\right)^2}d\theta \equiv \frac{1}{C_{kin}(g,t,\phi)}. \tag{4.11}$$

In equation 4.11, the function within the integral over θ yields two peaks, illustrated in figures 4.1(b) and 4.2. A relrod with $g < 2R_0$ enters the zeroth Laue 'bowl' once and then exits once as θ traverses 2π. The excitation error, describing the deviation from the Bragg scattering condition, traces a cosine curve shifted in the z-axis due to the curvature of the Ewald sphere and scaled depending upon distance of the reflection from the origin (equation 4.8). During the precession, reflections close to the origin are sampled slowly with smaller excitation error, so the shape of the modulus-squared of the sinc function along the θ-axis is widened and more intensity is sampled per unit time from low-$\mathbf{g}$ reflections than from high-$\mathbf{g}$ reflections. The higher-index reflections are more rapidly sampled, hence the squared sinc functions are very narrow in the

θ-axis. A large cone semi-angle ϕ increases the range of $\mathbf{s_g}$ over which the integration occurs, and in practice almost all reflections (except for very low indices) are rapidly sampled.

The model in equation 4.11 is useful as a starting correction, especially for thin specimens and large precession angle. However, apart from geometry errors, dynamical effects become prominent with increasing thickness, as evidenced in the lobstertail error plots in figure 3.9. In order to deal with specimens that are thicker, a more sophisticated model is needed to account for these effects.

4.1.2. Introduction of Two-beam Dynamical Excitation

When $\mathbf{s_g} = 0$, equation 4.9 reduces to $I(s_\mathbf{g}) = (\pi t/\xi_\mathbf{g})^2$, meaning the diffracted intensity can exceed the incident intensity when $t > \xi_\mathbf{g}/\pi$. This is not physical, and a better model is realized by considering the interaction of two beams propagating in a perfect crystal (Hirsch et al. 1965). The solutions to the analytical equations that describe this two-beam interaction are a pair of Bloch waves with relative magnitudes dependent upon the orientation of the crystal (e.g., the linear combination of the two must always meet the boundary condition at the exit surface).

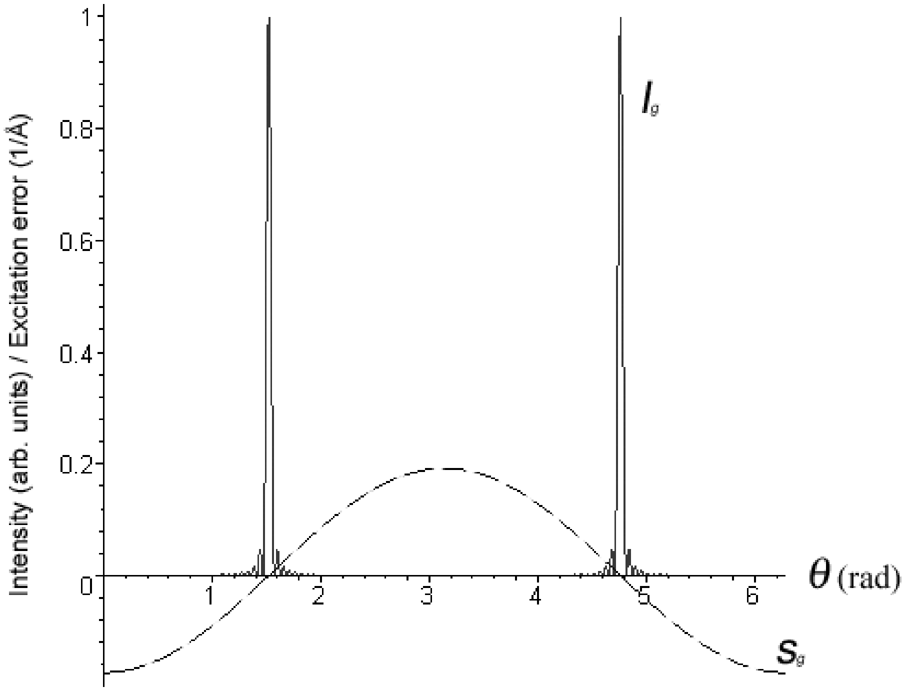

Figure 4.2. Intensity collected ($I_\mathbf{g}$) and excitation error ($s_\mathbf{g}$) during the integration in the kinematical model, plotted against azimuthal angle for a low-index reflection ($|\mathbf{g}| = 0.1R_0$, where $R_0 \approx \phi k = 0.96$ Å). Parallel illumination, with t = 100 Å, $\phi = 24$ mrad, 200 kV.

The scattered intensity is governed by a new deviation parameter called the effective excitation error, defined as

$$\mathbf{s}_{\mathbf{g}}^{eff} = \sqrt{\mathbf{s}_{\mathbf{g}}^{2} - \frac{1}{\xi_{\mathbf{g}}^{2}}}. \tag{4.12}$$

The effective excitation error modifies equation 4.9 to account for dynamical exchange between the transmitted and diffracted beams, giving

$$I(\mathbf{s}_{\mathbf{g}}) = \frac{1}{\xi_{\mathbf{g}}^{2}} \frac{\sin^{2}(\pi t s_{\mathbf{g}}^{eff})}{(s_{\mathbf{g}}^{eff})^{2}}. \tag{4.13}$$

When $\xi_{\mathbf{g}} > t$, the scattered intensity behaves like a conventional sinc function (with new scaling and periodicity — see the solid curve in figure 4.3). However, when $\xi_{\mathbf{g}} < t$, the scattered intensity at zero excitation error begins to fall, creating a minimum between two nodes centered about $s_{\mathbf{g}} = 0$ for some combinations of t and $\xi_{\mathbf{g}}$. The most dramatic change occurs when the argument of the sine function in the numerator of equation 4.13 becomes $n\pi$, where n is an integer (e.g., $\frac{t}{\xi_{\mathbf{g}}} = n$), at which point the scattered intensity at $\mathbf{s}_{\mathbf{g}} = 0$ falls to zero (dashed curve in figure 4.3).

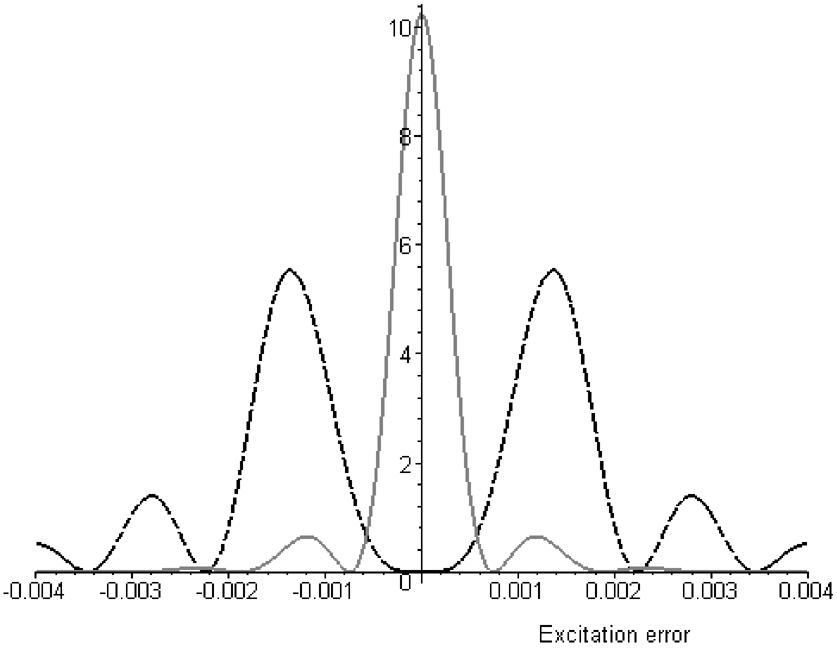

Figure 4.3. Scattered intensity ($I_{\mathbf{g}}$) v. excitation error ($s_{\mathbf{g}}$). Thickness $t = 500$. For the solid curve $\xi_{\mathbf{g}} = 1500$ Å and for the dashed curve $\xi_{\mathbf{g}} = 500$ Å (intensities not to scale). The binodal behavior occurs when $t > \xi_{\mathbf{g}}$.

The two-beam correction factor for precession thus comprises the integration along $\mathbf{s_g}$ of intensity profiles that vary with the extinction distance and specimen thickness (extinction distance is in turn inversely proportional to the structure factor). It models the exchange of intensity between the diffracted and transmitted beams and is valid when only one beam is strongly excited. Substituting 4.12 in 4.11, the exact two-beam correction factor is obtained:

$$\int_0^{2\pi} I(\theta)d\theta = \frac{1}{\xi_{\mathbf{g}}^2}\int_0^{2\pi}\frac{\sin^2(\pi t s_{\mathbf{g}}^{eff})}{(s_{\mathbf{g}}^{eff})^2}d\theta \equiv \frac{1}{C_{2beam}(g,t,\phi)}. \tag{4.14}$$

4.1.3. The Blackman Formula Revisited

In the early paper by Blackman (1939), the intensities of powder rings were elegantly described by two-beam dynamical theory. Using the same approach as presented in the previous section, the Blackman formula arises from a simple identity of the integrated scattered intensity. Equation 4.13 can be rewritten in slightly different form:

$$I_{\mathbf{g}} = I_0\frac{\sin^2 A_{\mathbf{g}}\sqrt{(W^2+1)}}{W^2+1}. \tag{4.15}$$

Here, I_0 is the incident beam intensity, assumed to be 1 in equation 4.13, $A_{\mathbf{g}} = \frac{\pi t}{\xi_{\mathbf{g}}} \propto F_{\mathbf{g}}t$, and $W = \mathbf{s_g}\xi_{\mathbf{g}}$. In powder and polycrystal diffraction, each constituent crystal is illuminated off of the zone axis by some angle ϕ, causing a corresponding excitation error for a given $\mathbf{g}$. A simple change of variables gives the excitation error as a function of this angle: $\mathbf{s_g} = 2k\theta\phi$. If the crystal is rocked with angular speed $\omega = \frac{d\phi}{dt}$, the total reflected intensity becomes

$$\begin{aligned} I^{tot} &= \frac{I_0}{\omega}\int_{-\infty}^{+\infty}\frac{\sin^2(A_{\mathbf{g}}\sqrt{(W^2+1)})}{W^2+1}d\phi \\ &\propto \frac{I_0}{2k^2\theta\omega}\frac{F_{\mathbf{g}}}{V_c}\int_{-\infty}^{+\infty}\frac{\sin^2(A_{\mathbf{g}}\sqrt{(W^2+1)})}{W^2+1}dW. \end{aligned} \tag{4.16}$$

The integration of the sinc function in equation 4.16 is equivalent to π times the integral from 0 to $A_{\mathbf{g}}$ of the zeroth order Bessel function. This identity gives the basic form of the Blackman formula:

$$\begin{aligned} I^{tot} = I_{\mathbf{g}}^{dyn} &= \frac{\pi I_0}{2k^2\theta\omega}\frac{F_{\mathbf{g}}}{V_c}\int_0^{A_{\mathbf{g}}} J_0(2x)dx \\ &\propto A_{\mathbf{g}}\int_0^{A_{\mathbf{g}}} J_0(2x)dx. \end{aligned} \tag{4.17}$$

It is important to note that the structure factors used to calculate $A_{\mathbf{g}}$ must be known as accurately as possible or the periodicity and amplitude of the integral will be altered. Figure 4.4 shows equation 4.17 plotted for the three strongest reflections in GITO. The strongest reflection has the greatest average intensity, and the average intensities decrease with decreasing structure factor. Note that in some thickness ranges such as 350-500 Å, the intensity of the strongest reflection drops below that of the next-strongest reflections.

The plots in figure 4.4 represent the Bessel integral for exact thickness values, however in real specimens there is usually some thickness variation Δt . The effect of thickness averaging on equation 4.17 in PED has previously been pointed out by Gjønnes et al. (1998b). In this model, Δt will generate a range of oscillation periodicities; superposition of scattered intensity from a range of thicknesses generates an effective curve that has reduced oscillation amplitude and slightly decreased intensity. The behavior at small $A_{\mathbf{g}}$, however, will remain essentially the same. In other words, the integral scales linearly with $A_{\mathbf{g}}$ regardless of thickness variation for small $A_{\mathbf{g}}$, but for large $A_{\mathbf{g}}$ the oscillations are damped and converge more rapidly to their final value when $\Delta t \neq 0$. This is advantageous because strong reflections will more likely maintain

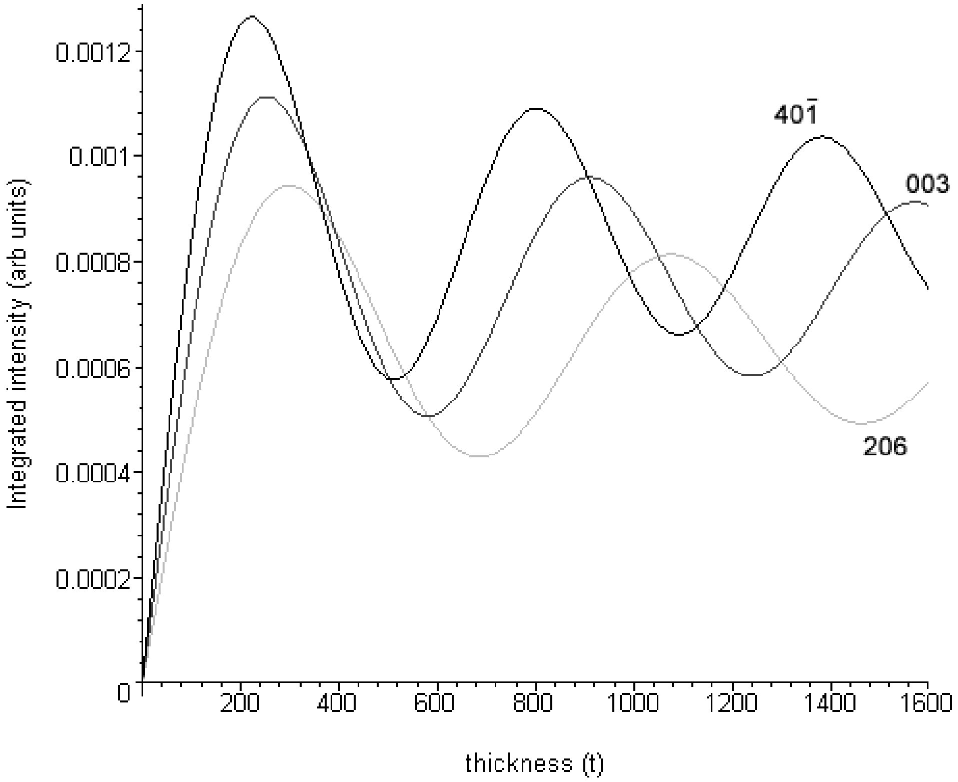

Figure 4.4. Equation 4.17 plotted for the three strongest reflections in GITO. The oscillation periodicities are slightly different because the extinction distance $\xi_{\mathbf{g}}$ varies between reflections. The extinction distances are 580 Å, 660 Å, and 780Åfor the 40$\bar{1}$, 003, and 206 reflections, respectively.

kinematical phase relationships between each other when there is some variation in thickness (recall equation 1.27).

4.2. Comparison between models

Five models of precession have now been discussed. To summarize, they are:

- Finite integration limits:
  - (1) Kinematical integral over $\mathbf{s_g}$ (Lorentz portion);
  - (2) Dynamical (two-beam) integral over $\mathbf{s_g}^{eff}$;
- Gjønnes form:
  - (3) Lorentz portion (approximation of (1));
  - (4) Lorentz and Blackman combined (approximation of (2); the Blackman portion has infinite integration limits);
- (5) Multislice (described in chapter 3).

Table 4.1 shows the different forms of the correction and some nomenclature by which to refer to them in the following sections. The fact that the Blackman formula also represents an integration of the two-beam condition is understood. However, for naming convenience, correction (2) will be denoted C_{2beam} while correction (4) will be denoted $C_{Blackman}$.

The multislice model is exact and effectively describes the physical behavior of PED, as demonstrated in section 3.2. Multislice will serve as the reference for comparing the approximate models listed above. We begin with a general discussion of their relationships, looking at trends from a theoretical standpoint. Later in this section, these relationships will be proven in practice by comparing the effectiveness of the correction factors at linearizing the simulated datasets.

4.2.1. Expected Trends

The integration limits along s_g are an important characteristic within the proposed models. Assuming for the time being that the scattered intensity in precession is always either kinematical or two-beam in nature (not n-beam where $n > 2$), the corrections C_{Gj} and $C_{Blackman}$ approximate the more exact corrections C_{kin} and C_{2beam} only if the precession has integrated nearly all of the scattered intensity. The conditions where this is satisfied are investigated below.

Figure 4.5 shows the behavior of the integral of the squared sinc function as a function of the integration limits. Most of the intensity is contained within the first period of the sinc function, and 98% of the intensity is sampled by integrating 5 periods. Beyond 5 periods, the integral converges toward unity more slowly, and 99% of the intensity is sampled only after integrating 10 oscillation periods. Depending upon the detector sensitivity and the amount of thickness averaging, experimental error is often within 3-5%, hence the integral can be considered complete as long as 5-10 periods are sampled *and* the sampled periods include the region near $\mathbf{s_g} = 0$. The latter constraint arises because the correction factors are inversely related to the integrated intensity; if only a tail of the squared sinc function is sampled, the

Table 4.1. Correction factors for correcting PED intensities. Note $C_{Blackman}$ has corrected integrand.

	Moniker	Type	Equation no.	Form
1	Finite kin	Goemetry only	4.11	$C_{kin}(g,t,\phi) = \left(\frac{1}{\xi_{\mathbf{g}}^2}\int_0^{2\pi}\frac{\sin^2 \pi t(s_{\mathbf{g}})}{(s_{\mathbf{g}})^2}d\theta\right)^{-1}$
2	Finite dyn	Full correction	4.14	$C_{2beam}(g,t,\phi) = \left(\frac{1}{\xi_{\mathbf{g}}^2}\int_0^{2\pi}\frac{\sin^2(\pi t s_{\mathbf{g}}^{eff})}{(s_{\mathbf{g}}^{eff})^2}d\theta\right)^{-1}$
3	Gjønnes	Geometry only	4.1	$C_{Gj}(g,\phi) = \mathbf{g}\sqrt{1-\left(\frac{\mathbf{g}}{2R_0}\right)}$
4	Gjønnes × Blackman	Full correction	4.1	$C_{Blackman}(g,t,\phi) = \mathbf{g}\sqrt{1-\left(\frac{\mathbf{g}}{2R_0}\right)}\frac{A_{\mathbf{g}}}{\int_0^{A_{\mathbf{g}}} J_0(2x)dx}$
5	Multislice	Exact	1.16	none (exact)

integrated intensity is very small and both experimental measurement and calculation become unreliable due to, respectively, insufficient signal-to-noise ratio and numerical error.

This behavior is still true when two-beam dynamical effects are introduced. The binodal curve that occurs when $t > \xi_{\mathbf{g}}$ exhibits the same behavior except the intensity within the tails does not damp as rapidly as in the squared sinc function (see the dashed curve in figure 4.3). The consequence is that a larger number of periods must be sampled for complete integration. The Blackman integral is a bipolar integration, therefore in order to apply it to precession data, all correction factors within the dataset must represent relatively complete integrations over both positive and negative excitation error.

To understand where the approximation $C_{Blackman}$ breaks down, it must be noted where the integration does not sufficiently sample the intensity scattered into the reciprocal lattice rods. Figure 4.6(a) shows the limits of the excitation error in the PED experiment. The minimum negative excitation error exceeds the maximum positive excitation error, and their ratio scales roughly with g. For example, the most positive excitation error occurs at the center of the Laue bowl when $g = R_0$ (reflection $\mathbf{g}$ in 4.6(a)), giving $s_{\mathbf{g}} = k(1 - \cos 0.024) \approx 0.012$ Å^{-1} for the experimental conditions of 200 kV and 24 mrad cone semi-angle (k is about 40 Å^{-1}). The most negative excitation error for reflection $\mathbf{g}$ is $s_{\mathbf{g}} \approx 0.035$ Å^{-1}. Typical extinction distances

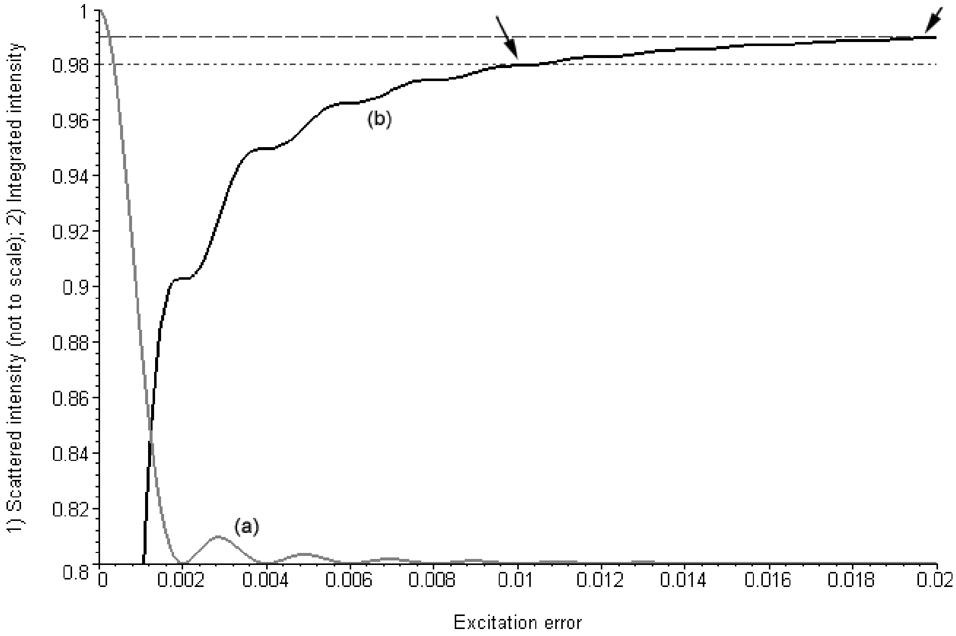

Figure 4.5. The squared sinc function (a) and the integral of the sinc function (b) plotted against excitation error for a crystal thickness of 500 Å. The integral converges rapidly toward unity as indicated by the arrows: 98% of the intensity is sampled when 5 oscillation periods are integrated, and 99% of the intensity is sampled by 10 oscillation periods.

for strong reflections are on the order of a few hundred Ångströms or greater, and crystal thicknesses are normally greater than 50 Å, giving an oscillation periodicity of < 0.005 Å^{-1} for the strongest reflections. Under these conditions, over a dozen periods of the shape function will be integrated as illustrated in figure 4.6(b).

The worst-case scenario occurs when the sinc-like function describing the scattered intensity has a large period in reciprocal space. This will occur when extinction distance (large structure factor) and specimen thickness are small, both on the order of 50 Å. This is very rare because the smallest $\xi_{\mathbf{g}}$ occurs for the strongest reflections, of which there are not many, and specimens are usually more than 200 Å thick. Recall the earlier example where the integration limits

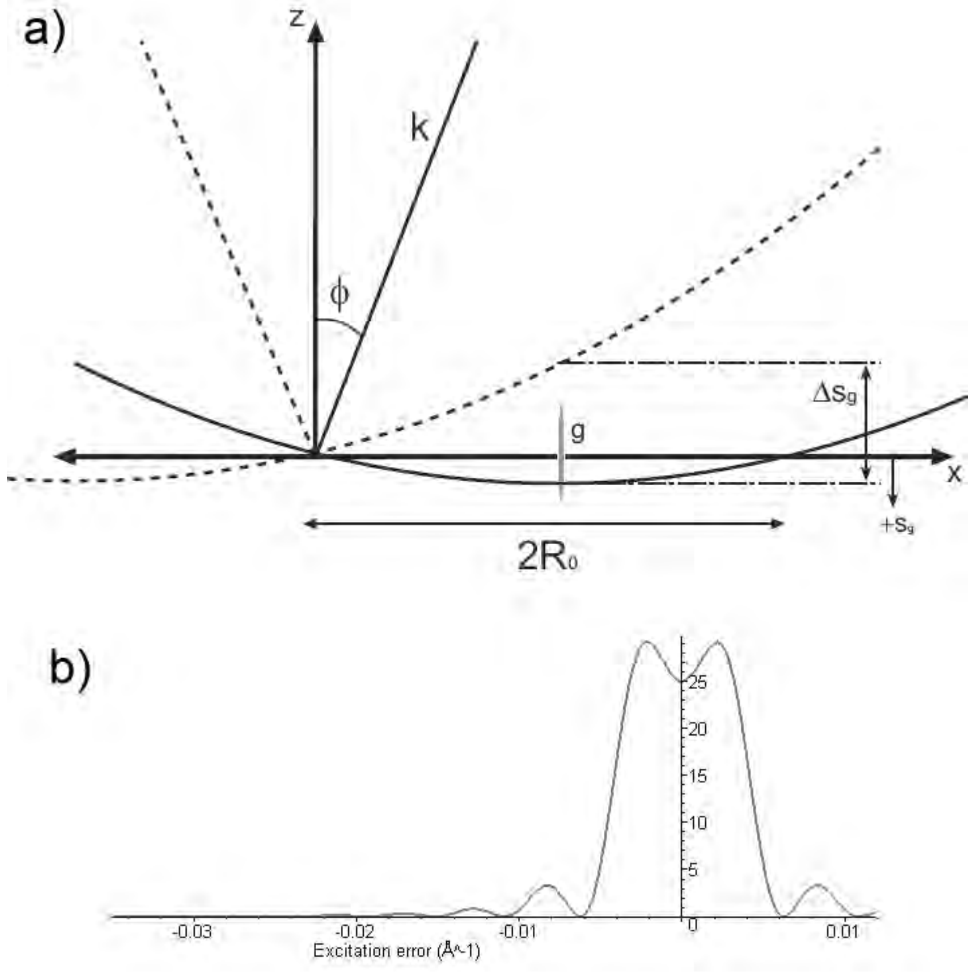

Figure 4.6. (a) The integration range $\Delta\mathbf{s_g}$ for reflection $\mathbf{g}$ located at $x = R_0$. Excitation error is positive in the $-z$ direction. (b) The scattered intensity over the range Δs from (a) for a crystal with $t = 200$ Å and $\xi_{\mathbf{g}} = 250$ Å.

were -0.035 Å^{-1} and 0.012 Å^{-1} for a reflection at $g = R_0$. For a material with $t = 250$ Å and $\xi_{\mathbf{g}} = 60$ Å, only about 7 oscillations will be integrated and the Gjønnes corrections will have greater than 15% error. For GITO, which has a very large unit cell volume, and correspondingly large extinction distance of 580 Å for its strongest reflection (index $40\bar{1}$), the intensity will be sufficiently integrated under most experimental conditions.

When $g > 2R_0$, positive excitation error does not occur. Corrections C_{Gj} and $C_{Blackman}$ break down beyond this point and are no longer applicable. However, the correction factors with finite integration limits (C_{kin} and C_{2beam}) will still be applicable slightly beyond $2R_0$ because the negative half of the sinc function is still integrable. Nevertheless, the correction factor will soon blow up beyond $2R_0$ and will be much less practical than simply extending the ZOLZ radius by increasing the cone angle ϕ (figure 4.7). In other words, the precession angle should be chosen such that the largest g of interest in the diffraction pattern is smaller than $2R_0$ by at least $0.25R_0$. Reflections with sufficient intensity to be measurable are typically within about 1.5 Å^{-1}, so ϕ = 20-25 mrad (at 200kV) is the minimum acceptable angle for PED studies where correction factors are applied.

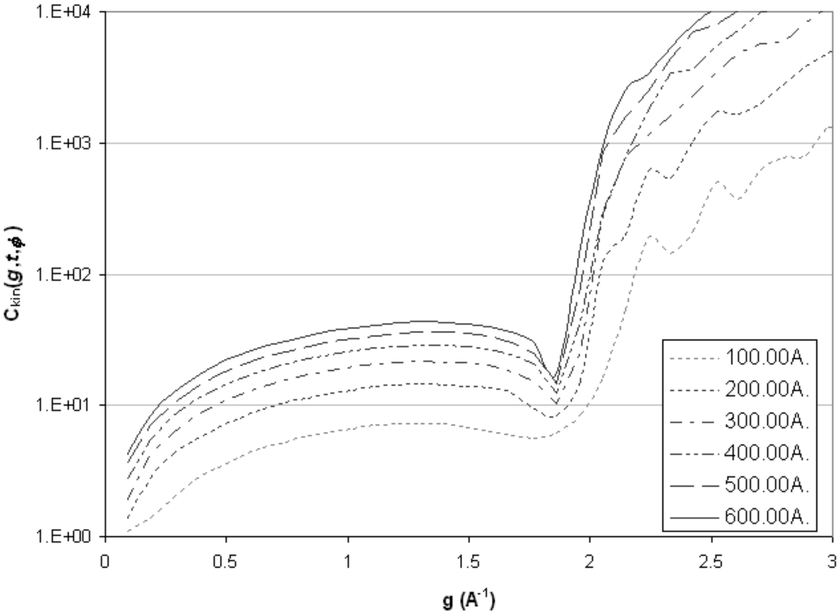

Figure 4.7. The kinematical correction factor C_{kin} for crystal thicknesses between 100 Åand 600Å, for $\phi = 24$ mrad. The correction factors behave nearly identically (with scaling) for $g < 1.8$ Å^{-1}, corresponding to about twice the radius of the zeroth order Laue zone ($2R_0$). Beyond $2R_0$, the correction factor is inversely proportional to the area within the tails of the relrod where there is very little scattered intensity, and the correction factor blows up.

Exploring cone angle selection further, recall that the structurally important reflections generally fall within the band $g = 0.25\text{-}1.5$ Å^{-1}, so it is advantageous to have larger cone angle to increase the positive limit of integration within this band (e.g., deepen the Laue bowl). Furthermore, recall from chapter 3 that going off-zone reduces simultaneous excitation of multiple strong reflections, thereby reducing amplitude errors in the PED dataset. Fortuitously, the constraints necessary for good integration coincide with the reduction of dynamical effects: large cone angle improves the correction factors by extending the integration limits along $s_{\mathbf{g}}$, and additionally reduces multiple scattering effects such that two-beam theory is adhered to better.

4.2.2. Comparison of Calculated Corrections Factors

The cases where the Gjønnes forms C_{Gj} and $C_{Blackman}$ deviate from the finite integration corrections C_{kin} and C_{2beam} will be illustrated first. Figure 4.8 shows C_{2beam} and $C_{Blackman}$ calculated for a number of thicknesses and tilt angles. Dynamical effects are reduced in thin crystals, so C_{2beam} and $C_{Blackman}$ (the full corrections) converge with the geometry-only corrections C_{kin} and C_{Gj}, respectively, in the limit of small t (applicable in figures 4.8(a)-(c)). Figures 4.8(a)-(c) represent small thickness, where the agreement between C_{2beam} and $C_{Blackman}$ models is poorest. A number of conclusions can be drawn from the figures:

- Small thickness produces a large oscillation period in the relrods, meaning that the integration along $s_{\mathbf{g}}$ is incomplete for many reflections. Therefore C_{Gj} represents a poor approximation to C_{kin}; in other words, $\mathrm{C}_{Blackman}$ does not match C_{Gj} for small t (figures 4.8(a)-(c)).
- Small cone semi-angle ϕ combined with small t results in the worst agreement between C_{2beam} and $\mathrm{C}_{Blackman}$ (figure 4.8(a)).
- Larger cone semi-angle improves the agreement between C_{kin} and C_{Gj} (figure 4.8(b)-(c)) due to larger integration limits along $s_{\mathbf{g}}$.
- The dynamical effects are reduced at small t, therefore Lorentz geometry dominates the correction factor. The tiny peaks on the $C_{Blackman}$ curve in figure 4.8(c) are dynamical corrections.
- $C_{Blackman}$ converges with C_{2beam} for larger thickness because periodicity in the relrod is small. Dynamical effects are accentuated, therefore a large correction is necessary for many reflections 4.8(d). For very large thickness, the dynamical correction is much larger than the geometry background.

As seen in chapter 3, the small thickness regime is where a correction factor is not strictly necessary; it is instead the large thicknesses (> 50 nm) where the correction factors are needed. For crystals with large thickness, the shape function has much smaller periodicity, so the integration within finite limits converges toward the integration over all excitation error and correction $C_{Blackman}$ is a good approximation to C_{2beam}. This agreement is demonstrated in figure 4.8(d): the whale-shaped background curve (Lorentz contribution) is consistent between

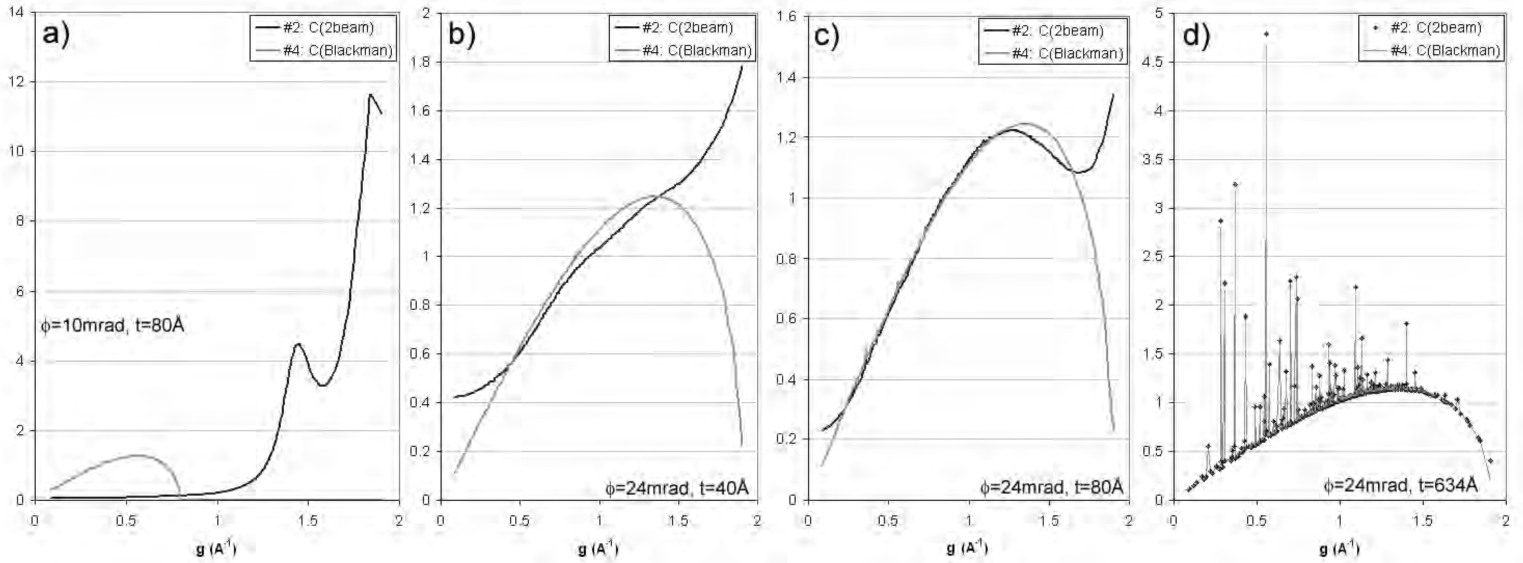

Figure 4.8. Comparison of the full correction factors C_{2beam} and $C_{Blackman}$ from table 4.1 plotted against g. (a)-(c) Dynamical effects are small when t is small, therefore the full corrections converge to C_{kin} and C_{Gj}, respectively. The plots show that C_{Gj} does not match the C_{kin} well at small thickness. (c) For larger tilt angle, Gjønnes-Blackman correction matches for $g < R_0$. Small peaks begin to appear on top of the geometry term (whale-shaped curve) as thickness increases. (d) Correction $C_{Blackman}$ matches correction C_{2beam} for large thickness because the periodicity within the relrod is very small. The dynamical corrections (peaks) dominate the correction factor values.

the two corrections at 634 Å, and the peaks match to within a few percent. Note that the corrections are plotted as curves to accentuate the peaking and the correction factors are not really continuous: each peak represents a correction for a specific reflection.

At large thickness, dynamical effects naturally begin to dominate. This is clearly seen in figure 4.8(d), where many reflections within the structure-defining regime 0.25-0.75 Å^{-1} have large corrections above the background curve. The key observation is that the correction factor *selectively* corrects reflections that have large error due to dynamical scattering. A second major point is that at large thickness, where relrods have small oscillation period, the geometry can indeed be separated from the thickness-dependent dynamical effects and the geometry can be approximated in the limit of moderate-to-large thickness by C_{Gj} which is independent of thickness. The net correction is reduced to the product between the Lorentz and Blackman terms.

Figure 4.9 shows the trends in more detail using plots of C_{2beam} for various thicknesses (increasing horizontally) and cone angles (increasing down each column). The thicknesses are large enough that $C_{Blackman}$ is a good approximation and will yield similar results for all plots except the top left ($\phi = 10$ mrad, $t = 32$ nm). Small cone angles yield incomplete integration of scattered intensity and the errors become substantial beyond $g = 2R_0$. The integration is fairly complete with larger cone angle, evidenced by the decay of dynamical-type corrections (spikes) at higher g within the plots. Large corrections are necessary for the reflections in the structure-defining range of 0.25-1 Å^{-1}. For very thick crystals (right-most column), dynamical effects extend out to very high spatial frequencies in the diffraction pattern, and their corrections extend to greater g correspondingly.

4.2.3. Application to Multislice Data Sets

The results from the previous analyses showed that $C_{Blackman}$ is a good approximation to the exact two-beam correction factor C_{2beam} in the thickness regime where a correction would be necessary ($> 10 - 20nm$). In *ab initio* structure studies, the structure factors necessary for either correction are not available, so the obvious tendency would be to apply a geometry-only correction. This approach requires only two pieces of information — an estimate of thickness and the cone angle — circumventing the need for forward calculation. Unfortunately, this proves to be a rather poor approach at the larger thickness regimes where the correction factors are needed. This seems counterintuitive, but the geometry correction is non-selective, so many intensities that need a large correction do not get the boost and weaker reflections can become too strong.

The kinematical Lorentz correction C_{kin} applied to simulated PED amplitudes is shown in figure 4.10 for thickness of 16, 32, and 63 nm. Refer to figure 3.8 for the uncorrected intensities. The amplitudes are slightly improved for 16 nm crystals, however there is no clear improvement for the 32 nm and 63 nm specimens. In thin crystals, almost none of the reflections have two-beam corrections. The weak reflections spread out along the z-axis for thick crystals because the dynamical corrections for the coupled beams have been omitted. Because there is not much

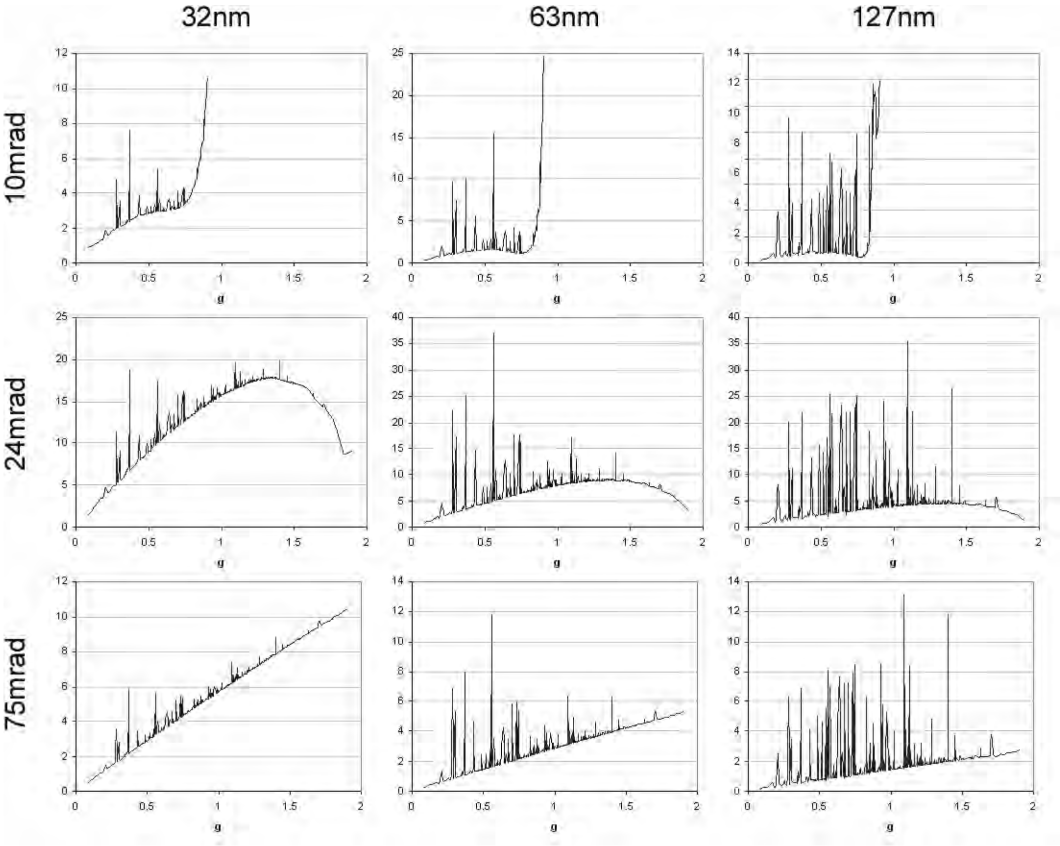

Figure 4.9. Tableau of correction factor plots for the GITO system calculated for various cone semi-angles and specimen thickness. The constituent plots represent C_{2beam} v. g. The plots in the 10 mrad row have a cutoff of $g = 0.9$ Å^{-1} because for small cone semi-angle the correction factor blows up at high spatial frequencies.

correlation between precession geometry and the beam intensity, the strongly coupled beams will receive insufficient correction under most circumstances.

This helps to explain why the R-factors were much worse in the Al_mFe and Ti_2P studies using intensities corrected only for geometry (Gjønnes et al. 1998a; Gemmi et al. 2003) versus the Al_mFe study utilizing the full correction (Gjønnes et al. 1998b). The reported R_1 values for the structures found using C_{Gj}-corrected intensities were 42% and 36%, respectively, versus 32% for the structure found using $C_{Blackman}$. The most uncertain step in the first two studies was the merging of multiple projections. This is to be expected with the crystal thickness on the order of 100 nm. The two-beam dynamical effects would be severe, and the reliability of scaling for common reflection is subject highly doubtful. The preferred solution is to simply use thinner crystals (e.g., fine probe near the specimen edge) and remove the reflections near the transmitted beam instead of treating the intensities for precession geometry.

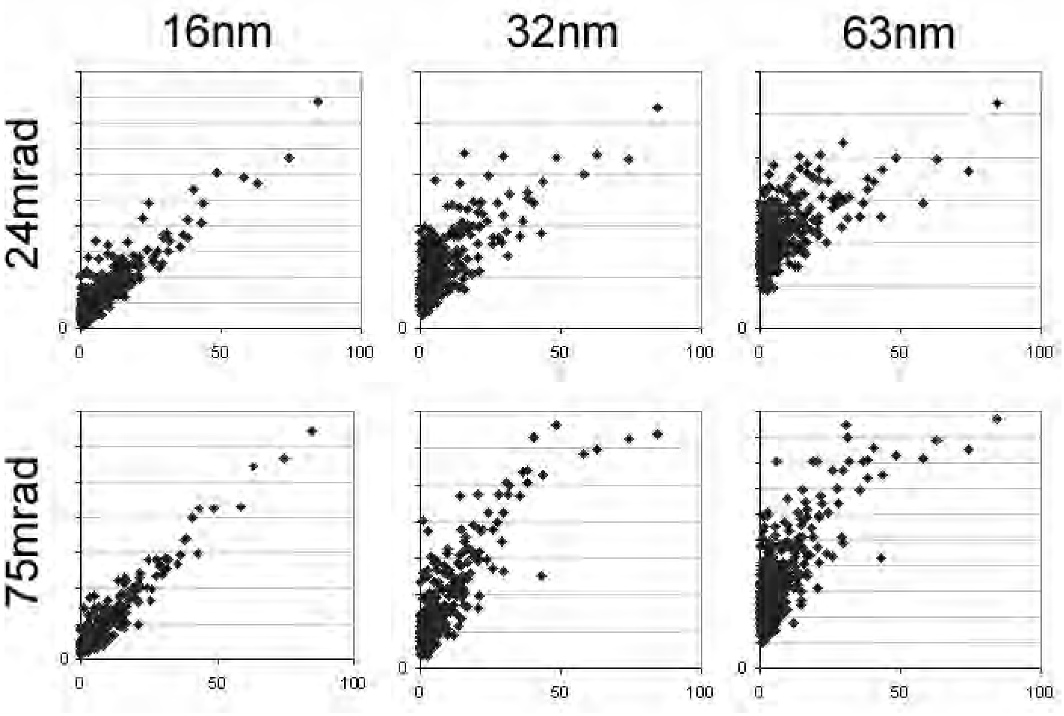

Figure 4.10. Multislice amplitudes with correction factor C_{kin} applied.

If structure factors are known, as in the case of partially-solved structures or where some structure factors have been obtained through other means such as CBED, then the C_{2beam} correction may be used. Figure 4.11 shows the application of the full corrections, some of which were shown in figure 4.9, to correct multislice amplitudes from figure 3.8. The top two rows of plots show that there is some divergence between C_{2beam} and $C_{Blackman}$ at small precession cone angle. This is less of a problem at large thickness, but in any case the error is not more than 10%. At larger cone semi-angles of 24 mrad and 75 mrad, C_{2beam} and $C_{Blackman}$ are virtually identical and only C_{2beam}-corrected plots are shown for those cone semi-angles.

The corrections work very well for thicknesses in the regime of 48-100 nm for the GITO structure. In this regime, the weak reflections still exhibit some residual offset, however the intensity ordering is very good. The residual offset occurs because there is always a small amount of multi-beam coupling around the ZOLZ ring and the stronger beams will always contribute some intensity to some of the weaker beams through short systematic paths. The strongest beams will be weakened slightly as they couple with the weakest beams surrounding them, giving rise to an apparent curvature in the amplitude reference plots. This effect is most pronounced in the 50-75 nm thicknesses.

At very large thickness (> 90 nm), the corrected intensities exhibit a minor inflection. This is a residual dynamical feature attributed to n-beam intensity exchange. The inflection is less

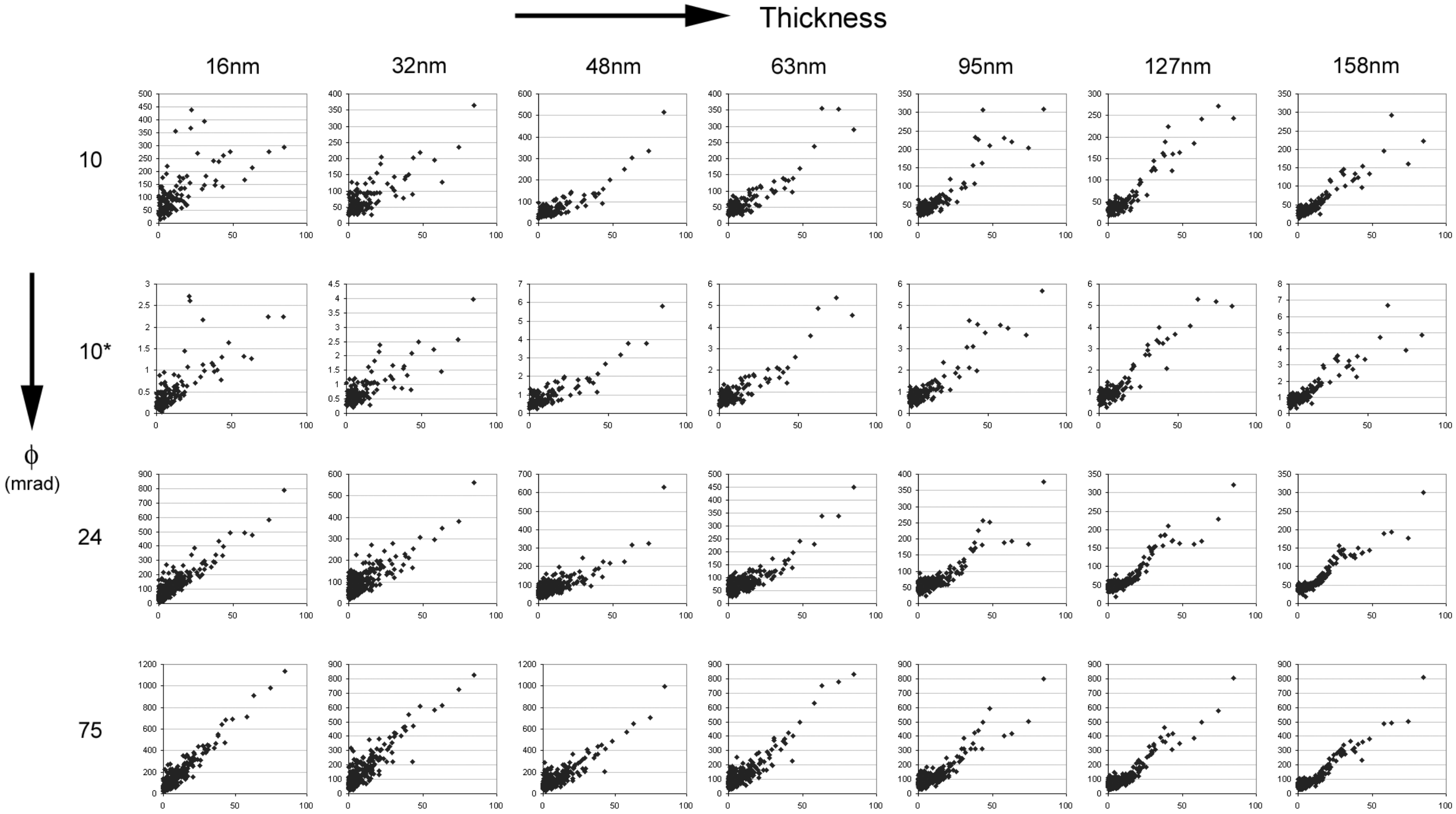

Figure 4.11. Plots of corrected amplitude v. kinematical amplitudes. Correction factors were applied to datasets simulated from multislice (200 kV). All plots use correction factor C_{2beam} except row 10*, which uses C_{Bk} (refer to table 4.1). 10 mrad corrected datasets include only $g < 0.8$ Å^{-1} due to the ZOLZ limit $2R_0$.

pronounced for $\phi = 75$ mrad, but occurs for a similar set of reflections (the strongest ones) regardless of changing experimental conditions. The inflected reflections all have extinction distance less than the specimen thickness and do not appear to lie in a specific band of g in the structure-defining range of 0.25-0.75 Å^{-1}.

The distribution of the reflections is shown expanded in figure 4.12 for the case of $t = 127$ mm, $\phi = 75$ mrad, and the indices of the strong reflections are labeled. The spread at low structure factor amplitude comprises weak reflections from the entire range, and reflections of varying spatial frequency ranges are distributed throughout, clearly indicating that the correction factors are applicable to reflections at all spatial frequencies. The nonlinear behavior evident in the corrected intensity shows that n-beam effects are still present, however the overall behavior of the dataset is linear. The fact that the inflected strong reflections span a range of g and do not seem to preferentially lie in a specific band of spatial frequencies indicates that the primary errors are due to weak dynamical excitations between neighboring beams and are not due to interaction between simultaneously-excited strong beams.

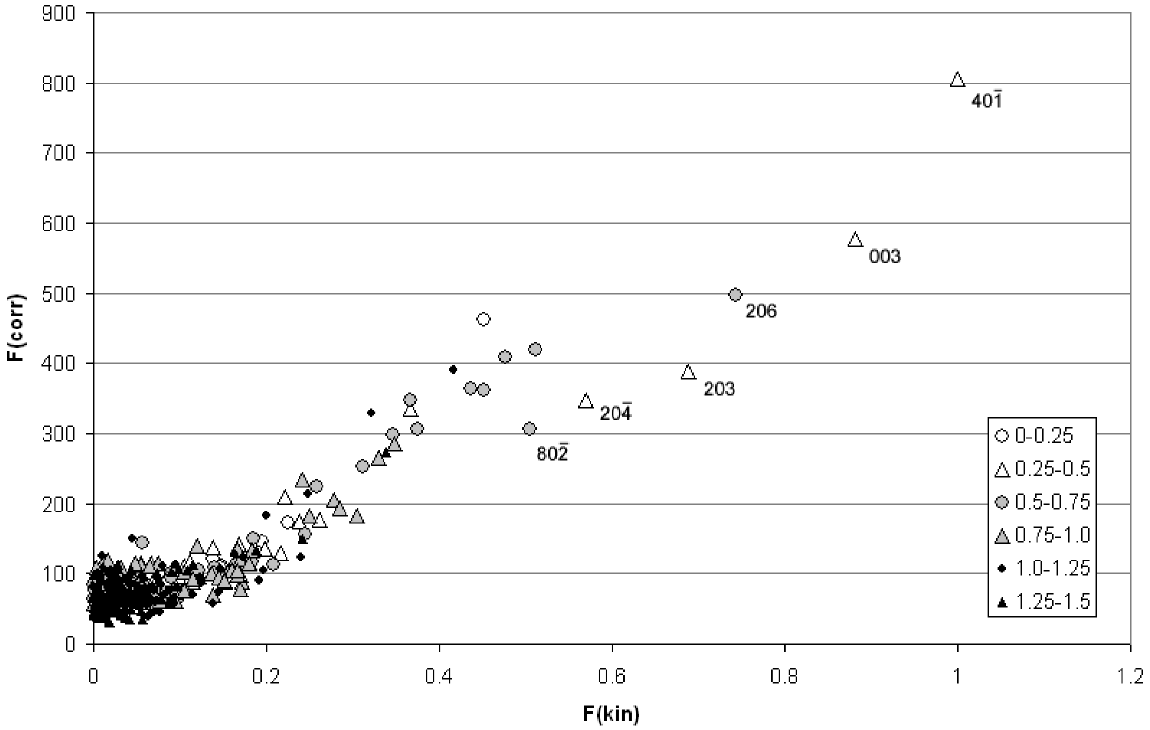

Figure 4.12. Detail plot of simulated intensities for $t = 1268$ Å corrected using C_{2beam}. The distribution of the intensities with g is indicated by symbol. Weak intensities from the entire range of g contribute to the spread at low amplitude, showing that dynamical effects are not strongly tied to spatial frequency (except in the continually multiply-excited condition near the transmitted beam).

An interesting exercise is to investigate the effect of error in the forward calculation. This is a crude test for the determining how well-conditioned the correction factor model is. Noisy structure factors were generated using the algorithm

$$F_{\mathbf{g}}^{noi} = \left(1 + \frac{e}{100} \times (n_{rand} * 2 - 1)\right) F_{\mathbf{g}}^{kin}, \tag{4.18}$$

where e is the percent error and n_{rand} is a random number between 0 and 1. The error introduced is bipolar and independent of the structure factor, so it is not intended to model dynamical effects. The R-factors for the structure factors with noise added are given in table 4.2. Each dataset had a different noise profile to control for any serendipitous correction behavior.

The datasets corrected with a C_{2beam} that has been calculated using the noisy structure factors were then plotted against the true structure factor. Figure 4.13 shows the corrected simulated datasets with largest noise profiles in the correction factors. R_1 values have been calculated for each set and are given in table 4.3. The R-factors of the corrected data shown in that table are much lower than the error contained within the inputted data. The improvement is, however, dependent upon the experimental conditions, which means that the geometry term plays a substantial role here. It is important to note that while the approach yields low R-factors, the plots in figure 4.13 indicate that the correction factors do not strongly preserve intensity relationships. This is to be expected, since there is no way that equation 4.14 can predict the correct structure factor. However, the moderately well-conditioned character of this algorithm does make way for a potential iterative correction factor scheme, wherein a poor starting set of structure factors might be refined into more accurate structure factors by applying *a priori* constraints and then refining based upon a statistical two-beam dynamical model.

We conclude this section with the mention that the mechanism behind some of the residual dynamical behaviors are not manifestly obvious. For example, the R-factor is lower for larger thickness (also observed qualitatively in figure 4.11). This might be explained by the fact that the integral over excitation error converges to a constant in the limit of large t. Under this condition, the correction factor behavior is dominated by the prefactor $1/\xi_{\mathbf{g}}$. In other words, equation 4.1 (which holds within the very large thickness regime) becomes

Table 4.2. R_1 for the structure factors with noise added using equation 4.18.

Thickness	10% error	20%error	40%error
	— 24 mrad —		
400	9.734	20.122	41.498
800	9.800	21.315	39.140
	— 75 mrad —		
400	10.492	20.103	40.601
800	10.077	19.266	40.528

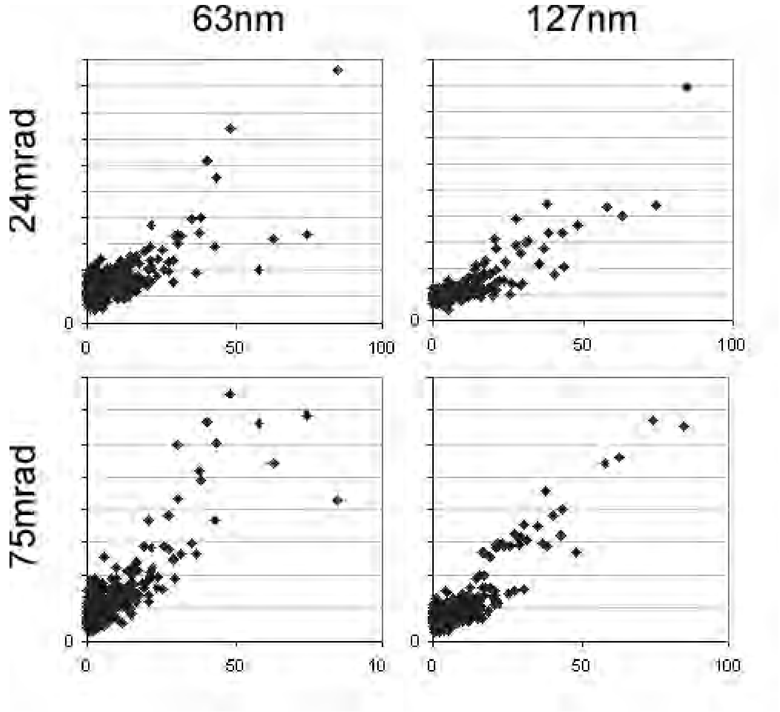

Figure 4.13. Multislice datasets corrected with C_{2beam} using structure factors with 40% noise added. The abscissa within each plot represents the true kinematical structure factor. R-factors for these plots are given in table 4.3.

Table 4.3. R_1 for C_{2beam}-corrected intensities using noisy structure factors. Table values in percent.

Thickness	10% error	20%error	40%error
	— 24 mrad —		
400	9.370	9.398	9.501
800	6.991	6.977	7.019
	— 75 mrad —		
400	15.337	15.480	15.622
800	12.716	12.694	12.807

$$I_{\mathbf{g}} \propto F_{\mathbf{g}} I_{\mathbf{g}}. \tag{4.19}$$

Most intensities, except for the weakest ones, are in the regime of large $A_{\mathbf{g}}$ where the Bessel integral has converged, resulting in a more consistent behavior. Also, surprisingly, the R-factors for $\phi = 75$ mrad are worse than for $\phi = 24$ mrad. This is counter to the trends seen so far, which almost universally show that large precession cone angle is favorable. The exact mechanism behind this is not clear and requires further analysis in a future study.

4.3. Discussion: Approach for Solving Novel Structures

For precession to become a reliable and widespread technique for generating good starting structure models from electron diffraction data, it must be fast and consistent. Chapter 3 showed that it is natively psuedo-kinematical for small-to-moderate thickness regimes, with primary errors in the range of $g < 0.25$ Å^{-1}. PED offers a new working range of up to 40-50 nm crystal dimension, representing a very favorable regime for dealing with real-world bulk structures. The next step, covered in detail within this chapter, has been to extend the capabilities to even greater thickness by means of correction factors.

It has been shown here that if structure factors are known, the correction generated by a two-beam dynamical model is quite successful up to extraordinary thickness (beyond 160 nm). This result proves that PED adheres very closely to two-beam dynamical scattering, especially at large thickness and large precession angle. It also shows that the data are affected by n-beam effects, as seen in the structure factor plots where there remain some residual nonlinearities that depend upon thickness. The effects, however vary systematically with increasing experimental thickness and angle, and are slowly varying with changing experimental conditions.

The two-beam dynamical model, while fairly accurate, is unfortunately not immediately practical for generating an *a priori* correction factor for general use. This is because successful correction for large thickness requires a forward calculation: the structure factors must be known before the crystal structrure can be solved. Nevertheless, the analyses do give some new tools for enhancing *ab initio* structure solution using PED and open the way toward less complex iterative structure solution methods than multislice, which requires both structure factors and phases.

The structure solution in chapter 3 on GITO already made use of a crude form of the correction factors that were investigated in this chapter. In section 3.1 a simple modification was made to the experimental precession data from GITO (figure 3.4(a)) that appeared to linearize the measured amplitudes to a kinematical approximation. This simple approach involved using the square of the amplitudes — the intensities — instead of the amplitudes to solve with direct methods. The structure maps that were generated from this procedure had identical atom positions to the solution found using high-pass filtered amplitudes, however it more clearly displayed some of the atom positions (e.g., clearer peaks) that were very close to the noise floor in the amplitude solution. This is an interesting behavior for which an explanation is not manifestly obvious.

The underlying principle can be found by examining the limits of the Blackman formula 1.24. By rearranging the Blackman equation, the measured intensity $I_{\mathbf{g}}^{dyn}$ from a crystal of greater than moderate thickness ($t > 25$ nm) becomes

$$I_{\mathbf{g}}^{dyn} \propto F_{\mathbf{g}}^{kin} \int_0^{A_{\mathbf{g}}} J_0(2x)dx. \tag{4.20}$$

In the limit of large $A_{\mathbf{g}}$, the integral converges to a constant of 0.5. Therefore, when the thickness is very large or if **g** is a strong reflection,

$$I_{\mathbf{g}}^{dyn} \propto F_{\mathbf{g}}^{kin}. \tag{4.21}$$

In effect, even though not all reflections necessarily obeyed equation 4.20, the important reflections (the strong ones) did and became more linearized toward pseudo-kinematical values. The fact that weaker reflections might not obey equation 4.20 offers a mechanism as to why the background in figure 3.6 contains noisy oscillations.

In *a priori* investigations of novel structures, a clear path for how to treat the data has now been elucidated. There is overwhelming evidence that large cone semi-angle ϕ is beneficial to the quality of the data. Additionally, thin specimens are advantageous because they decrease error, and the thinnest ones ($<$ 15 nm) are easy to treat via a kinematical correction for geometry. The geometry corrections C_{kin} and C_{gj}, counterintuitively, are not favorable. The low spatial frequency reflections contained in the range $g < 0.25$ Å^{-1}, which are usually weak, exhibit the largest dynamical error because they are near the transmitted beam and are almost always undergoing simultaneous excitation with other beams during the precession experiment. Unless important reflections lie within that range for the structure under investigation, they should be high-pass filtered regardless of whether correction factors are used.

The requirement for forward calculation is an unfavorable one because precession is still not able to solve novel structures from data that is taken from very thick specimens. The effects are slowly varying with thickness if a large hollow-cone angle is used, and complementary methods can indicate the approximate thickness regime. Therefore, the conditions giving rise to large dynamical errors in the data can usually be avoided. The major breakthrough from this chapter is that there is strong evidence showing that the structural electron crystallography problem has been reduced from a many-beam problem to a largely two-beam. This is a major simplification and future methods, keeping in mind that $|F_g|$ is all that is required for the forward calculation, will need to take advantage of this new understanding.

The methods presented in chapter 3 should give favorable starting structure solutions for structures that project well, e.g., they exhibit the property that intensities that have been linearized to a pseudo-kinematical approximation. The use of intensities rather than amplitudes is advantageous in the moderate-to-large thickness range (t = 25-75 nm) if used with large cone angle. This method must, however, be used with caution since dynamical behaviors in uncorrected intensities may be substantial at the top of the thickness range for some materials. A classic example is where two neighboring reflections are both strong: a clear path for strong dynamical exchange exists in such a case. Reflections near the transmitted beam predictably contain the largest dynamical errors, and in *a priori* structure studies it is recommended that those reflections be removed using high-pass filtering except in cases where such beams are structurally important, such as for very large superstructures. A flowchart describing a suggested procedure is given in figure 4.14.

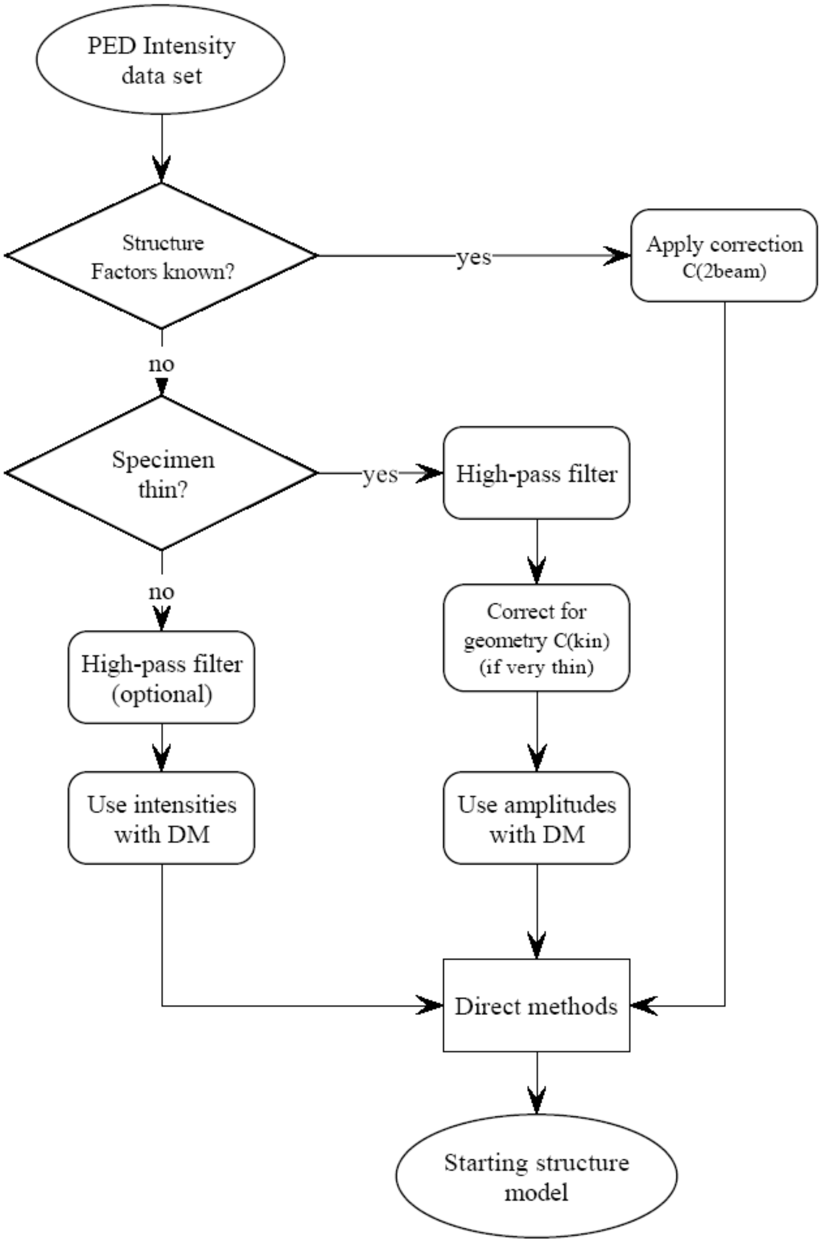

Figure 4.14. Flowchart for generating a starting structure model from a PED data set.